

Journal of Materials Chemistry A

Accepted Manuscript



This is an *Accepted Manuscript*, which has been through the Royal Society of Chemistry peer review process and has been accepted for publication.

Accepted Manuscripts are published online shortly after acceptance, before technical editing, formatting and proof reading. Using this free service, authors can make their results available to the community, in citable form, before we publish the edited article. We will replace this *Accepted Manuscript* with the edited and formatted *Advance Article* as soon as it is available.

You can find more information about *Accepted Manuscripts* in the [Information for Authors](#).

Please note that technical editing may introduce minor changes to the text and/or graphics, which may alter content. The journal's standard [Terms & Conditions](#) and the [Ethical guidelines](#) still apply. In no event shall the Royal Society of Chemistry be held responsible for any errors or omissions in this *Accepted Manuscript* or any consequences arising from the use of any information it contains.

1 **Hygrothermal simulation-informed design of mesoporous desiccants for optimised**
 2 **energy efficiency of mixed mode air conditioning systems**

3

4 Fernando Sarce Thomann ^{a*}, Matthew R Hall ^{a, b}, Robert Mokaya ^c, Lee A Stevens ^a

5 ^a *Division of Materials, Mechanics and Structures, Faculty of Engineering, University of*
 6 *Nottingham, University Park, Nottingham, NG7 2RD, UK*

7 ^b *British Geological Survey, Environmental Science Centre, Keyworth, Nottingham, NG12*
 8 *5GG, UK*

9 ^c *School of Chemistry, University of Nottingham, University Park, Nottingham, NG7 2RD, UK*

10

11 *corresponding author - Email: emxf@s@nottingham.ac.uk; Tel: +44 (0)115 8467873

12

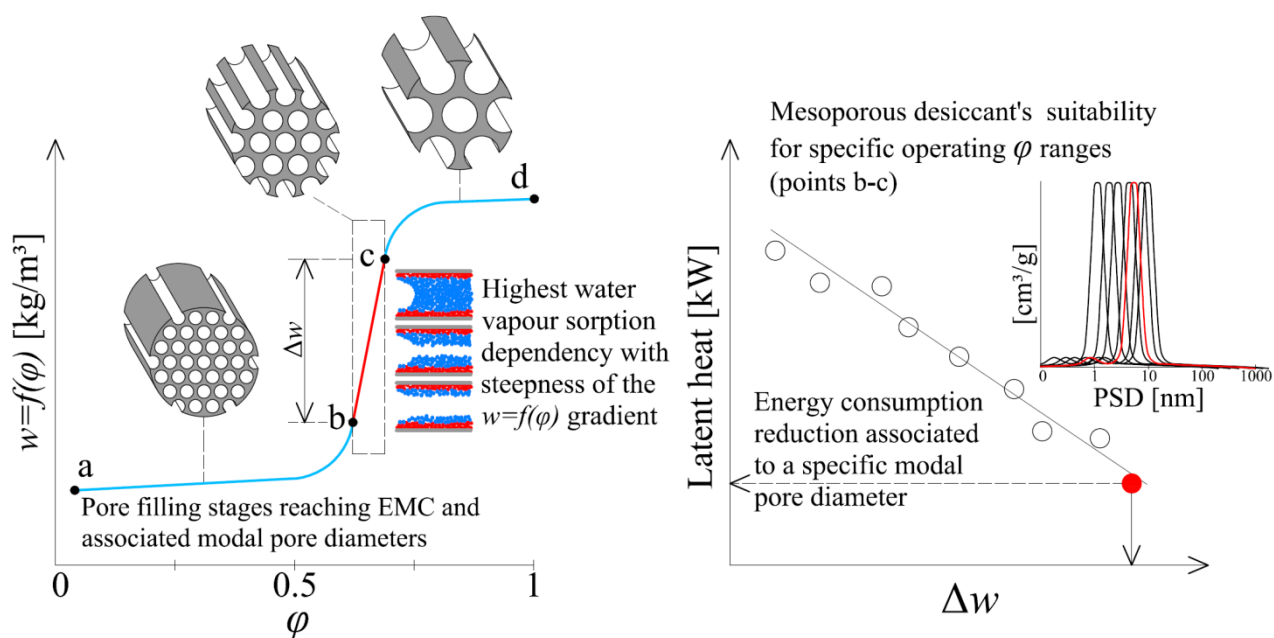
13

14

15

16

17



18

19

20

21 **Abstract**

22 This paper describes an optimization technique using hygrothermal numerical modelling to
23 determine an ideal and unknown isotherm in order to inform the design of optimised
24 mesoporous desiccants. Their suitability for passive humidity buffering as well as their impact
25 on energy efficiency was assessed when assisting a mixed mode air-conditioning (AC)
26 system. Three clear stages of water vapour adsorption were found that strongly correspond to
27 the Δw gradient when assessing the kinetics of adsorption and exchange rates for periodic
28 moisture loads. Consistent agreement was found between the latent heat of dehumidification
29 used by the AC system and the desiccant decay time after successive sorption loop cycles.
30 This confirmed the material's suitability for specific applications and was found to be highly
31 sensitive to the portion of the isotherm between $\varphi_{i,L} - \varphi_{i,U}$ (Δw gradient), compared with full
32 adsorption capacity (total w) when assessing total energy consumption. The experimental
33 results of sorption kinetics appeared to be slightly underestimated between the Δw gradient
34 and the response time to reach equilibrium moisture content (EMC). The major
35 underestimations were found to be consistent with the kinetics of adsorption/desorption when
36 analysing their significance based on w differences. These were largely attributed to a
37 combination of adsorption kinetics (time-response) and adsorption/ desorption hysteresis.
38 However, this was not evident when comparing long-term experimental data and numerical
39 estimations for water vapour sorption isotherms, since numerical model accurately predicted
40 them. This suggests that both adsorption kinetics and the scanning curve prediction, within a
41 hysteresis loop, are not accurately represented by current hygrothermal models and are hence
42 a priority for future research.

43

44 **Keywords:** hygrothermal modelling; water vapour isotherm; desiccants design; mesoporous;
45 air conditioning; energy efficiency

46

47

48

49 **Nomenclature**

50	ρ	Bulk density	kg/m ³
51	c_p	Specific heat capacity	J/(kg K)
52	$\lambda(w)$	Moisture-dependent thermal conductivity	W/(m K)
53	ϕ	Relative vapour pressure (p_v/p_{sat})	-
54	n	Bulk porosity	m ³ /m ³
55	$w = f(\phi)$	Water vapour sorption isotherm	kg/m ³
56	$\mu(\phi)$	Water vapour diffusion factor	-
57	$D_w(w)$	Liquid water diffusivity	m ² /s
58	RH	Relative humidity; where RH = $\phi \cdot 100$	%
59	p_v/p_0	Partial pressure of water vapour	-
60	H	Total enthalpy	J/m ³
61	h_v	Latent heat of phase change	J/kg
62	t	Time	s
63	T	Temperature	K
64	δ_p	Vapour permeability	kg/(m s Pa)
65	Suffixes:		
66	i	interior	
67	e	exterior	
68	L	lower limit	
69	U	upper limit	

70

71

72 1 Introduction

73 Desiccant material performance is typically assessed with respect to isotherm characteristics
74 and target application^{1,2}. This implies that the criteria for optimisation are dependent upon
75 the thermal and moisture loads, and operating parameters, inside the closed environment
76 being studied. Optimised mesoporous desiccants can be used to passively regulate indoor dry
77 bulb temperature and relative humidity in closed environments, and to reduce the energy
78 penalty of mechanical heating, ventilation and air conditioning (HVAC)^{3,4}. Traditional
79 refrigerant vapour compressor systems (VCS) used for regulating the interior psychrometric
80 conditions of ‘closed environments’ (*e.g.*, offices, hospitals, laboratories, industry, *etc.*) are
81 responsible for a large amount of energy consumption with associated greenhouse gas
82 emissions⁵⁻⁸. The study of desiccants as dehumidifier materials in the air-conditioning (AC)
83 industry has attracted the interest of many researchers in the last decades⁹⁻¹³. This has
84 primarily motivated the understanding their abilities to reduce the ‘energy penalties’ caused
85 by mechanical air dehumidification (latent heat), and the required energy to reheat the air up
86 to the supply air temperature (sensible heat), by engineering their water adsorption/retention
87 properties¹⁴⁻¹⁷. Some examples of desiccant implementation are included in (i) AC mixed
88 mode systems^{18,19}, (ii) evaporative cooling technology for high humidity climates^{20,21}, (iii)
89 regulating indoor thermal comfort²²⁻²⁴, (iv) as a solid–desiccant in solar AC systems²⁵⁻²⁸, (v)
90 indirect evaporative cooling systems^{29,30}, and (vi) waste heat transformation applications for
91 absorption chillers and heat pumps³¹⁻³⁴.

92

93 As an alternative to traditional VCS cooling technologies, solid–desiccant cooling systems
94 (SDC) have motivated the investigation of advanced desiccant materials since their
95 characteristics (water adsorption behaviour, regeneration capacity, and long–term stability)
96 play an important role in their performance and efficiency^{35,36}. These have been organized
97 into three main categories³⁷: (i) composite desiccants (*i.e.*, silica-based, mesoporous silicate-

98 based and carbon-based), (ii) nanoporous inorganic materials (*i.e.*, aluminosilicate zeolites,
99 aluminophosphates, and aerogels), and (iii) polymeric desiccants (*i.e.*, metal–organic
100 frameworks (MOFs) and polyelectrolyte). Ongoing research^{38–42} has been focused on the
101 preparation of these materials with improved water adsorption characteristics which include
102 high surface area, large pore volume and an unprecedented physicochemical variability. This,
103 in the case of MCM-41 and SBA-15, has been possible due to the modulation of their textural
104 properties through the synthesis process by controlling temperature^{43, 44} and reaction time^{45,}
105⁴⁶. These mesoporous materials exhibit enhanced water adsorption properties compared with
106 those traditional silica–based as a result of having regular pore structures and high surfaces
107 areas⁴⁷. On the other hand, significant interest has been focussed on MOFs as water
108 adsorbents due to their large adsorption capacity, fine–tunable pore size, high surface area,
109 and pore volume controlled by change in organic ligands and metal sub–units^{48–51}. In recent
110 work done by Furukawa *et al.*⁵², large water adsorption capacity and pore volume (735–850
111 cm³ g⁻¹ and 0.88 cm³ g⁻¹, respectively) was reported from low to high p_v/p_0 range (0.05–0.7).
112 Their MOF materials exhibited outstanding sorption/desorption water uptake after 5 cycles
113 (showing no loss of porosity) at a low regeneration temperature (25 °C). In addition, studies
114 done in Materials of Institute Lavoisier (MIL) frameworks showed even greater values of
115 water adsorption (1.06–1.7 cm³ g⁻¹) and large pore volume (1.4–1.58 cm³ g⁻¹)^{53–55} with low
116 regeneration temperature (30 °C), and rapid–response rates of 40 % weight loss after only 30
117 minutes at 30 °C⁵⁵. It is expected that desirable properties in an optimal desiccant material
118 are therefore not only its water adsorption capacity (and isotherm type), but also their rate of
119 sorption/desorption (kinetic stability) at a defined regeneration temperature.

120

121 All of these desiccants have currently only been analysed in terms of full adsorption capacity
122 (*i.e.*, independent of isotherm shape) with the intention of producing large pore volumes, and
123 have not assessed their suitability for specific applications. In order to do this an

124 understanding of the isotherm shape at particular p_v/p_o ranges is required, as well as their
125 transient response to changes in ambient vapour pressure, Δp_v . If understood, advanced
126 desiccant materials could then be used to partially or even fully regulate the fluctuations of
127 RH and to allow reduction in energy penalties when tailoring and optimizing their isotherm
128 shape for regulating ‘specific’ psychrometric requirements of closed environments. Therefore,
129 the aim of this study was to apply a numerical hygrothermal approach (from our previous
130 work ⁵⁶) to determine the ideal (and unknown) water vapour isotherm to inform the design of
131 optimised mesoporous desiccants. The isotherms were then experimentally re-created through
132 synthesis and modulation of well-known mesoporous material classes (MCM-41 and SBA
133 15). The material’s suitability for regulating indoor RH, in terms of dehumidification load
134 reductions (enthalpy), were assessed after different moisture loads had been introduced. They
135 were then assessed to enable the relative effect on energy efficiency when assisting a mixed
136 mode air conditioning (AC) system. The sorption/desorption kinetic response of selected
137 traditional and advanced desiccants will be then assessed experimentally.

138

139 **2 Experimental section**

140 **2.1 Desiccant Candidates**

141 A set of ten candidate desiccants (see Figure 1) were selected as part of a representative group
142 of mesoporous materials, as defined by IUPAC ⁵⁷. The aim was to assess their capacity for
143 buffering humidity ratio fluctuations (and hence indoor air enthalpy) within specific closed
144 environment scenarios. In recent work a principle was established which defined the available
145 moisture capacity, Δw for RH buffering within a specific operating range ⁵⁶. Therefore, the
146 region of interest among the isotherm candidates was defined between point *b* seen in Figure
147 2a (1st inflection point; the onset of multilayer physisorption) and point *c* (2nd inflection point;
148 the percolation threshold). The capillary transport coefficients (D_{ws} and D_{ww}) were calculated

149 from each isotherm⁵⁸, and the water adsorption coefficient, A was assumed constant for all
150 materials based on assumptions established from previous work³⁸.

151

152 2.2 Synthesis and characterization

153 Synthesis and the textural properties of the pure silica MCM-41@165 were obtained using
154 same experimental description of our previous work⁵⁶. Synthesis of SBA-15 (6 nm pore size)
155 was prepared in a similar manner to Zhao *et al.*⁵⁹ with the same batch of SBA-15 used
156 throughout the study. Pluronic 123 (P123, triblock copolymer (EO)20(PO)70(EO)20, 80.0 g)
157 was dissolved in aqueous hydrochloric acid (1.33M, 3000 ml) with vigorous stirring at 35 °C.
158 After complete dissolution tetraethoxyorthosilicate (TEOS, 182 ml) was added dropwise and
159 the mixture stirred at 35 °C for 24 h. The solution was then statically heated at 85 °C for 48 h.
160 The resulting white solid was dried in an oven at 105 °C for 2 h before heating in a furnace to
161 600 °C for 6 h to obtain a white solid powder. Synthesis of SBA-15 (10 nm pore size) was
162 prepared in a similar manner to Zhao *et al.*⁵⁹ with the same batch of SBA-15 used throughout
163 the study. Pluronic 123 (P123, triblock copolymer (EO)20(PO)70(EO)20, 4.0 g) was
164 dissolved in aqueous hydrochloric acid (1.33 M, 75 ml) and mesitylene (2 ml) with vigorous
165 stirring at 35 °C. After complete dissolution tetraethoxyorthosilicate (TEOS, 4.55 ml) was
166 added dropwise and the mixture stirred at 35 °C for 24 h. The solution was then placed in a
167 Teflon lined autoclave and heated at 120 °C for 24 h. The resulting white solid was recovered
168 and then in an oven at 105 °C for 2 h before heating in a furnace at 600 °C for 6 h to obtain a
169 white solid powder. Textural properties (see Table 1) were determined from N₂ sorption
170 analysis at -196 °C using a Micromeritics ASAP 2020 analyser. Samples (approximately 0.2
171 g) were outgassed prior to analysis under high vacuum at 120 °C for 15 h. Specific Surface
172 areas (SSA) was calculated using the standard Brunauer–Emmett–Teller (SBET) method,
173 micropore volume (V_m) by the t–plot method with Harkins and Jura correction for thickness
174 curve correction. Average pore diameter (D_p) was determined by the Barret–Joyner–Halenda

175 (BJH) method by applying a cylindrical pore model using Kelvin equation with Harkins and
176 Jura for thickness curve correction. Nitrogen adsorption at relative pressure of 0.99 was taken
177 as total pore volume (V_p).

178

179 2.3 Dynamic Vapour Sorption (DVS)

180 A gravimetric dynamic vapour sorption (DVS) test was performed to determine the water
181 vapour isotherms for the candidate materials (MCM-41@165, SBA-15 6 nm and SBA-15 10
182 nm). A DVS Advantage-2 series (Surface Measurements Systems Ltd., London, England)
183 with incorporated ultra-microbalance (1 μ g sensitivity) and fully automated weighing/purging
184 was used to independently control T_{db} and RH to an accuracy of ± 0.5 K and ± 1.5 %,
185 respectively (vapour pressure accuracy ± 1.5 % p_v/p_0). Advantage Control Software (ACS)
186 was used to automatically record the data in 1 min time-steps. Before analysis, the samples
187 were dried under vacuum at 120 °C for 12 h to ensure removal of residual moisture. In order
188 to ensure stability for baseline measurements accuracy, clean quartz sample and reference pan
189 were left to fully equilibrate at 23 °C at constant nitrogen flow (10 sccm 1 bar) for 1 h prior to
190 the weighing and tared. Dry samples (approximately 0.2 g) were weighed into the sample pan
191 and allowed to equilibrate again under the carrier gas for 1 h. After stability, the sample
192 weight was recorded (initial mass M_0) and reference weight was set to zero with no counter
193 weight. To ensure $w = 0$, a pre-heating sequence was set from 23 to 150 °C (2 °C/min
194 ramp rate) for 1 h prior to vapour dosing. A targeted relative vapour pressure from $\phi = 0.05$
195 to 1 ($\phi = 0.05$ intervals) was programmed to sequentially increase in a 21-steps full cycle
196 (sorption/desorption), where a change in mass step (0.001 %/min) was set until EMC was
197 achieved. This was performed at T_{db} 23 °C and to a constant water vapour flow rate of 100
198 sccm.

199

200 Three sets of experiments to assess the water vapour adsorption/desorption kinetics were
201 performed. For this, a set of RH limits were defined (20–30 %; 30–50 %; and 50–70 %) and
202 the kinetics of the moisture sorption began to sequentially fluctuate in an
203 adsorption/desorption cycle. Each cycle comprised 2 h of moisture sorption (*i.e.*, 30–50 %
204 RH) followed by 2 h of moisture desorption (*i.e.*, 50–30 % RH) for a total period of 12 h (3
205 complete cycles). Prior to testing, all samples were outgassed under vacuum at 120 °C for 12
206 h and the pre-heating sequence was applied as described above. To ensure that EMC was
207 achieved for the w_{20} , w_{30} and w_{50} set points, all samples were pre-conditioned within the DVS
208 chamber before the cycles started. Taring and equilibration of the microbalance steps were
209 done as previously described, where all samples (~ 0.02 g) were loaded to define the initial
210 mass (M_0) in the DVS. This was performed at T_{db} 23 °C at a constant water vapour flow rate
211 of 100 sccm, as with previous experiments.

212

213 2.4 Hygrothermal numerical model

214 A number of hygrothermal models packages have been validated over the past 15 + years
215 against experimental data including (but not limited to) DELPHIN, HAM, MATCH and
216 WUFI⁶⁰, as part of the Annex 41 project⁶¹. To validate numerical model predictions for heat
217 and mass transport/storage physical model are commonly used to simulate the bulk-scale of
218 the hygrothermal behaviour of some functional material properties⁶²⁻⁶⁴. As a minimum, all
219 hygrothermal numerical models must accurately predict the following bulk-scale coupled
220 phenomena of heat and mass transport/storage⁶⁵:

221

- 222 • heat storage in dry materials and any absorbed water
- 223 • heat transport by moisture-dependent thermal conduction
- 224 • latent heat transfer by vapour diffusion
- 225 • moisture storage by vapour sorption and capillary forces

- 226 • moisture transport by vapour diffusion
- 227 • moisture transport by liquid transport (surface diffusion and capillary flow)

228

229 For this study, the *Wärme und Feuchte Instationär* (WUFI) hygrothermal numerical model⁶⁰,
 230 WUFI+ v2.5.3 (Fraunhofer, Germany), was used. The governing equation that represents the
 231 moisture storage function is seen in the LHS of Eq. 1, which is proportional to the derivative
 232 of the water adsorption isotherm ($\partial w/\partial \varphi$). The transport terms on the RHS of Eq. 1 are
 233 described by the divergence of liquid and vapour diffusion with phase changes strongly
 234 dependent on the moisture fields and fluxes. Whilst the driving potential for vapour flux,
 235 which is vapour pressure ($p_v = \varphi \cdot p_{sat}$), is strongly temperature-dependent (saturation pressure
 236 $p_{sat} \sim \exp(T)$). The liquid flow, on the other hand, is governed by differences in capillary
 237 forces which are assumed to be a function of RH only (*i.e.*, from Kelvin condensation). The
 238 storage term seen in LHS of Eq. 2 describes the vapour enthalpy of air flow inside the closed
 239 environment, whilst the RHS describes heat transport due to solid conduction and diffusion of
 240 heat associated with the specific enthalpy of vapour water.

241

$$242 \text{ Moisture balance: } \frac{dw}{d\varphi} \cdot \frac{\partial \varphi}{\partial t} = \nabla \cdot (D_w \nabla \varphi + \delta_p \nabla (\varphi \cdot p_{sat})) \quad \text{Eq. 1}$$

$$243 \text{ Energy balance: } \frac{dH}{dT} \cdot \frac{\partial T}{\partial t} = \nabla \cdot (\lambda \nabla T) + h_v \nabla \cdot (\delta_p \nabla (\varphi \cdot p_{sat})) \quad \text{Eq. 2}$$

244

245 2.5 Sensitivity analysis

246 Sensitivity analysis was conducted to assess the water vapour adsorption behaviour (capacity)
 247 and water vapour exchange performance for all candidate materials in a closed environment
 248 where the initial moisture content was $w = 0$. The hygrothermal numerical model was setup to
 249 sequentially perform water vapour adsorption simulations between the operating limits $\varphi_{min} =$
 250 0 and $\varphi_{max} = 0.95$. A moisture generation rate of 3 g/h per 24 h period with an air
 251 infiltration rate of 0.35 ACH h^{-1} were set. The water vapour exchange rate was then estimated

252 as the fraction of cumulative moisture load per hour. The closed environment comprised a
253 thermally and hygrically isolated box (where $V = 1 \text{ m}^3$) with the initial boundary conditions
254 (interior/exterior) were set at $\varphi_i = 0$ and $\varphi_e = 0.95$ under isothermal conditions, $T_{db} = 23 \text{ }^\circ\text{C}$.
255 The fabric of the envelope comprised a 2 mm thick vapour barrier ($S_d = 1500 \text{ m}$) and 240 mm
256 thick vacuum insulation panel ($\lambda = 0.001$). A non-visualized internal component was defined
257 (area/volume ratio = 0.4048 m^2 , equivalent to $\sim 500 \text{ g}$) comprising 2 mm thickness of
258 candidate material and using the hygrothermal functional properties detailed in Table 2. These
259 were gathered from previous research³⁸, where pore geometry and specific surface area were
260 obtained using the BJH and BET method with N_2 physisorption. Validation against high
261 resolution transmission electron microscopy (HRTEM) and small-angle X-ray diffraction
262 (SAXRD) were conducted. Modified transient plane source (MTPS), differential scanning
263 calorimetry (DSC) and dynamic vapour sorption techniques were used to determine the
264 hygrothermal functional properties. The numerical model was solved using (i) increased
265 accuracy and adapted convergence options, (ii) time step 1 min, ‘fine’ mesh grid spacing, and
266 (iii) calculation accuracy of 0.5 %/0.5 $^\circ\text{C}$ for RH and T_{db} , respectively.

267

268 2.6 Parametric studies

269 Parametric hygrothermal simulations were conducted to determine the fluctuation of $\varphi(t)$ and
270 the candidate material’s capacity for humidity buffering in a series of closed environment
271 scenarios. Each material was parametrically assessed against five pairs of operating limits
272 ($\varphi_{min}-\varphi_{max}$); *i.e.*, 0.4–0.5; 0.5–0.6; 0.6–0.7; 0.7–0.8; 0.8–0.9. The initial moisture content, w
273 was set according to the φ_{min} limit at EMC; *i.e.*, w_{40} , w_{50} , w_{60} , w_{70} , and w_{80} . A number of
274 moisture loading cycles, N was set comprising 12 h moisture generation (at a rate of 3 g/h)
275 followed by 12 h of no moisture generation (24 h total), *i.e.*, 22 cycles in total. The air
276 infiltration rate (0.35 ACH h^{-1}) and φ_e were constant, with the latter value determined
277 according to the φ_{min} limit (*i.e.*, $\varphi_e = 0.4, 0.5, 0.6, 0.7, \text{ or } 0.8$) and to a constant dry bulb

278 temperature, $T_{db} = 23$ °C. The non-visualized component thickness and area/volume ratio,
279 fabric components, and parameters for the numerical model were set as described in Section
280 2.4. Expanded numerical simulations were then conducted to quantify the operational energy
281 used for dehumidification loads (enthalpy energy) and cooling demand, with the candidate
282 materials assisting a mixed mode AC system. The upper indoor dry bulb temperature set
283 point, ($T_{dbi,U}$) was set as $T_{dbi} \geq 25$ °C, and the upper indoor air humidity set point (ϕ_{max}) was
284 defined for each pair of operating limits ($\phi_i \geq 0.5, 0.6, 0.7, 0.8, 0.9$), as previously described.
285 In order to simulate instantaneous control response, 50 kg/h of dehumidification capacity and
286 50 kW cooling capacity were assumed for the AC system. Once the ϕ_{max} and $T_{dbi,U}$ set points
287 had been achieved, and if any of the operational limits were exceeded, the ratio of
288 dehumidification or cooling demand could be estimated and the relative effect on energy
289 efficiency calculated. This commonly occurred in cases where the moisture loads were always
290 positive, *i.e.*, where no infiltration of air at lower relative moisture content occurred. For each
291 candidate material, the initial value of w was set according to the ϕ_{min} limit, *i.e.*, EMC at w_{40} ,
292 w_{50} , w_{60} , w_{70} , and w_{80} . A constant air infiltration rate (0.35 ACH h^{-1}) was used, and the
293 moisture load was derived from the resultant outdoor air moisture content at $\phi_e = 0.95$ at $T_{db} =$
294 23 °C. The non-visualized component thickness and area/volume ratio, fabric components,
295 and parameters for the numerical model were set as described in Section 2.4. The initial
296 boundary conditions were, however, set equally for interior operating limits ($\phi_{min}-\phi_{max}$), and
297 $\phi_e = 0.95$ at $T_{db} = 23$ °C. The numerical model setup was later adjusted to simulate the
298 kinetics of the water vapour uptake by sequentially fluctuating the adsorption/desorption cycle
299 across an arbitrary sixty cycles ($N = 60$). Each material was parametrically assessed using the
300 same RH limits as for the DVS experiments in Section 2.2 (20–30 %; 30–50 %; and 50–70
301 %), where the initial w was set accordingly (*i.e.*, EMC at w_{20} , w_{30} and w_{50}) and $T_{db} = 23$ °C. A
302 constant ACH = 20.37 h^{-1} and area/ volume ratio (0.01) of the non-visualized component
303 were determined. This was to enable scaling between the DVS chamber volume ($V_{ch} =$

304 0.0002945 m^3) and the numerical model ($V = 1 \text{ m}^3$), assuming an infiltration rate of 100 sccm
305 ($0.006 \text{ m}^3 \text{ h}^{-1}$) and material quantity of 0.02 g. This enabled validation of the numerical model
306 against the DVS experiments.

307

308 **3 Results and discussion**

309 **3.1 Continuous moisture load sensitivity analysis**

310 Figure 3 clearly shows three stages of water vapour adsorption as w reaches equilibrium
311 moisture content (EMC), where each stage was identified within a specific portion of the
312 isotherm as depicted in Figure 2a. The first stage (schematically sketched in Figure 2b)
313 between points a and b represents an early saturation stage of the materials in the first 48 h
314 where a steep ϕ gradient was found. In the cases of MIL-101⁶⁶, PS-C16-R⁶⁷ and SBA-15, the
315 higher Δw gradient during adsorption between $\phi = 0$ to *ca.* 0.4, and desorption between 0 to
316 *ca.* 0.9 resulted in a less pronounced curve and a small but significant delay when achieving
317 the 1st inflection point b . A second stage was a sub-plateau between point b and c where a
318 characteristic stabilized ϕ_i corresponded to the highest Δw at the 2nd inflection point c , *i.e.*, the
319 percolation threshold. The slope of the sub-plateau indicates its dependency upon the
320 steepness of the $w: p_v/p_0$ gradient corresponding to maximum pore volume. Previous work has
321 demonstrated that the positive correlation between the moisture storage capacity (Δw) and the
322 optimum ϕ operating range for a given isotherm can also be identified⁵⁶. Almost all samples
323 exhibited the sub-plateau segment in their isotherms, which started from point b (onset of
324 multilayer physisorption between $\phi = c$. 0.35–0.90), with the exception of the Aerogel⁶⁸. This
325 suggests a prolonged capillary conduction stage. In the third stage between points c and d , a
326 rapid increase in ϕ_i was observed with noticeable variation towards EMC_{100} , especially in
327 materials having type V isotherms (*e.g.*, KIT-1⁶⁹). The progressive reduction in pore volume
328 strongly affected the time taken to reach inflection point d towards EMC_{100} , as a consequence
329 of the low Δw on that portion of the isotherm. Evidence of this was found for MCM-41@180

330 ⁵⁶, which was the first to achieve EMC_{100} (112 h) and has the lowest pore volume (0.53 g cm^{-3})
331 ³). However, it was apparent that by having a greater Δw between points c and d , the elapsed
332 time before reaching EMC_{100} was significantly increased. Evidence of this was found when
333 comparing KIT-1 (152 h) and FSM-16 (168 h) ⁶⁹, both with similar Δw at point c (460 kg m^{-3})
334 ³), but with the latter having a steep $w: p_v/p_0$ gradient resulting in a higher Δw above $\varphi = 0.7$
335 ($\sim 44 \text{ kg m}^{-3}$).

336

337 3.2 Water vapour exchange performance

338 Figure 4 shows the cumulative water vapour uptake for all candidate materials. The same
339 correlations were observed in Section 3.1 for stage 1–3 water vapour adsorption and the
340 corresponding portions of the isotherm (see Figure 2). It appears that in the first stage (points
341 a and b) there is an ‘apparent’ high initial water vapour uptake (relative to $w = 0$) followed by
342 a visible depression caused by early saturation. This applied to MCM-41, KIT-1, FSM-16,
343 and Aerogel. Note that in the cases of MIL-101, PS-C16-R and SBA-15 the cumulative water
344 vapour adsorption was clearly higher (between 84 % to 99 %) and controlled by the higher
345 initial Δw gradient between points a and b (see Figure 2a). After this stage, a sub-plateau was
346 observed in the second stage (points b and c , with the highest Δw gradient), which
347 corresponded to maximum pore volume. Here some materials (MIL-101, PS-C16-R and
348 SBA-15) reached 100 % of the cumulative water vapour uptake. Once point c of the isotherm
349 was reached the moisture content (with respect to pore volume) was sufficiently high for
350 performance to begin to decay after successive internal moisture load cycles. This indicates
351 moisture content dependency and reduced water vapour adsorption ability prior to reaching
352 w_{100} from point c of the isotherm. Figure 5a shows a positive linear correlation between the
353 moisture storage capacity, w and the water vapour being exchanged (against time) with the
354 absorbent. However, Figure 5b shows that the relationship between w and the time taken to
355 exceed the φ_{max} limit ($\varphi = 0.95$) correlates more strongly with type V isotherms ($R^2 = 0.99$)

356 compared with type III isotherms ($R^2 = 0.77$). This could partially be explained by the
357 observation that the process of water vapour adsorption was triggered early by a capillary
358 condensation stage on Type III isotherms. Therefore, SBA-15 10 nm and Aerogel material do
359 not fit trend line A since their capillary potential and capacity for water vapour adsorption are
360 already lowered.

361

362 3.3 Water vapour buffering simulations

363 Figure 6a–b shows the RH buffering results for repeated long-term loop cycling (at $N = 12$) of
364 all material candidates. The operating range ($\varphi_{min}-\varphi_{max}$) of each test was 0.4–0.5 and 0.7–0.8,
365 respectively. The absence of water vapour buffering can be seen followed by an early decay
366 process which correlates to the first stage of water vapour adsorption between points a and b
367 of the isotherm (Figure 2a). This sudden decay relates to the smaller Δw gradient seen in
368 Figure 7a, causing the material to fail after N number of cycles when the fluctuation of $\varphi(t)$
369 exceeds the φ_{max} limit (Figure 7b). From Figure 7b it is apparent that the progressive decay
370 until material failure corresponds with the largest proportion of water vapour adsorption (see
371 Figure 7a) in each operating range. The most suitable candidate materials for each range can
372 be identified as that with the longest time before exceeding the φ_{max} limit. This suggests that
373 the sub-plateau segment (see y -axis displacement in Figure 3) is sensitive both to x -axis
374 adjustments in the sorption isotherm (*i.e.*, pore size distribution) and to the value of Δw (w :
375 p_v/p_0 gradient) between $\varphi_{i,L}-\varphi_{i,U}$ limits.

376

377 3.4 Air dehumidification and energy consumption

378 Figures 8a–c show the ratio of dehumidification loads removed by the materials once they
379 achieve the φ_{max} set point on the mixed mode AC system (repeated for ranges between: 40–
380 50; 60–70; and 70–80 % RH). The steepness of the curve was found to be dependent on the
381 time required to achieve the corresponding EMC (*e.g.*, EMC_{50} as seen in Figure 8a). This

382 supports the idea that total control (100%) from the AC system corresponds to the lower Δw
383 gradient, whereas a plateau (at 0 %) means that the indoor moisture load was fully regulated
384 by the desiccant by having a higher Δw gradient. In all cases, it can be recognized that a
385 higher elapsed time before the inflection of the curve start there is a corresponding material
386 that fits within the optimum operating ranges; for example, MIL-101 and PS-C16-R ($\varphi = 0.4$ –
387 0.5), MCM-41@150⁵⁶, KIT-1, and FSM-16 ($\varphi = 0.6$ –0.7), and all MCM-41 types ($\varphi = 0.7$ –
388 0.8). Once the inflection point starts (above 0 %; see red circles in Figure 8a) in the sub-
389 plateau region, the adsorbent progressively has lower potential to fully regulate φ ; and air
390 dehumidification starts to operate.

391 Figure 9 shows a significant difference between the resultant indoor RH(t) and the material's
392 RH(t) in all simulations. Since the adsorbent appears not to have achieved EMC (*i.e.*, EMC₅₀–
393 70–80) a distinctive offset between both curves was observed. This suggests that the material
394 may continue adsorbing water vapour whilst the φ_{min} set point on the AC is still
395 dehumidifying the indoor air, and hence working in true mixed mode.

396

397 Figure 10 shows a positive linear correlation between the moisture sorption capacity (Δw
398 gradient) and the latent heat used for air dehumidification for each specific operational range.
399 This satisfactorily proves that passive regulation of RH fluctuations in a specific closed
400 environment can fully be controlled by materials where a higher Δw gradient is found whilst
401 consuming less energy. This was previously evidenced in Figures 9–11, where reduction of
402 the dehumidification loads removed by the HVAC system was strongly related to a higher Δw
403 gradient corresponding to materials that fit within the optimum operating ranges. Consistent
404 agreement was also observed between the decay (up to material failure) and the latent heat of
405 dehumidification, wherein the most suitable candidate materials can be identified in Figure
406 7b. A significant increment in the resultant indoor air temperature was observed in some cases
407 (*e.g.*, MIL-101 and PS-C16-R), most likely due to heat of adsorption. As a result, an extra

408 cooling load was added to both MIL-101 and PS-C16-R (*i.e.*, 0.22 and 0.16 KW respectively)
409 in order to maintain isothermal conditions ($T_{dbi} = 23$ °C). Figure 11 shows the total energy
410 used for air dehumidification (latent heat) and the energy used for cooling purposes (Figure
411 11a), and no correlation trend ($R^2 = 0.2706$) between total moisture storage, w and total latent
412 heat for air dehumidification (Figure 11b). In the latter case, it can be seen that having higher
413 w (*e.g.* Aerogel, MIL-101, PS-C16-R and SBA-15 10 nm) does not result in lowering the
414 energy used for dehumidification purposes when assuming total pore volume capacity.
415 Evidence of this can be seen when comparing the total latent heat used for type V and type III
416 isotherms; *e.g.*, MCM-41@180 (1.51 kW and $w = 369.4$ kg m⁻³) and Aerogel (1.65 kW and w
417 = 754.8 kg m⁻³), with the latter having w ~2 times higher compared to MCM-41@180. These
418 results provide evidence for the premise in which adsorbents are expected to fully operate
419 under total adsorption capacity, independent of isotherm shape, rather than for specific
420 applications and p_v/p_0 scenarios.

421

422 3.5 Experimental work and model validation

423 Figure 12 compares the experimental DVS and numerical simulations (water vapour
424 sorption/desorption kinetics) for the three newly synthesised materials (MCM-41@165, SBA-
425 15 6 nm and SBA-15 10 nm). The upper and lower % RH buffering limits were defined as
426 20–30 % RH; 30–50 % RH; and 50–70 % RH in Figure 12. Experimentally, it appears that for
427 all materials EMC (red dotted line in Figure 12) was achieved at $N = 3$ for cases where the Δw
428 gradient was sufficiently small (a, b, d, e, and g) with respect to the relevant portion of each
429 sorption isotherm (see Figure 1). Additionally, it appears that the kinetics for
430 sorption/desorption within the % RH buffering limits was highly sensitive to the Δw gradient.
431 This corresponded to a rapid response (steep adsorption/desorption curve) for the smallest Δw
432 gradient. Evidence of this was found in MCM-41@165 operating at 20–30 and 30–50 % RH
433 (see red boxes in Table 3). In all other cases it was evidenced by a less steep

434 sorption/desorption curve and corresponding to those with a higher Δw gradient. To some
435 extent, the numerical predictions seen in Figure 12 (a, b, d, e, and g) appear to be slightly
436 underestimated (solid black line) towards the time in achieving EMC, especially in those
437 between Δw_{20-50} (see Table 3). This is normally found in numerical models due to the lack of
438 a dynamic input for w , with respect to the time-response for water vapour adsorption at partial
439 EMC; *i.e.*, w inputs are assumed to be at full EMC for single sorption isotherms. Further
440 analysis confirmed that the average difference (%) between experimental and numerical w
441 data for all sorption cycles was significantly attributed to this; *e.g.*, MCM-41@165 with
442 43.4% within the Δw_{30-50} cycle seen in Table 4. In the case of those having greater w between
443 the upper and lower % RH buffering limits (c, f, h, and i from Figure 12), it is suggested that
444 for both experimental and numerical data, their capacity for water vapour adsorption is
445 significantly beyond the required time period for achieving EMC (see Table 3). Besides, for
446 all candidates seen in red circles (Figure 12), there appears to be a combination of time-
447 response together with a hysteresis phenomenon. The latter, can be recognized by the highest
448 average (%) values at the end of the third cycle shown in Table 4 (see a, c, d, and g). In both
449 adsorption and desorption cycles, this could be largely due to the presence of scanning curves
450 within the hysteresis loop. However, the corresponding loops at this stage are unidentified.
451 Conversely, there is close agreement (full sorption/desorption reversibility) when a smaller
452 Δw gradient is found; for example, SBA-15 10 nm operating in the 50–70 % RH ranges (see
453 Figure 12i). This could be explained because SBA-15 10 nm showed the lowest average
454 difference between experimental and numerical w data (see Table 4 – 7.6%), which indicates
455 a high degree of sorption/desorption reversibility (and small hysteresis -4.6%). On the other
456 hand, numerical data of the final EMC were accurately predicted (refer to Section 3.1),
457 suggesting that there is some level of variance between short and long periods for water
458 vapour adsorption/desorption kinetics. This perhaps indicates a need for further research in
459 which the concept of time-response for water vapour adsorption, hysteresis loops and the

460 associated scanning curves can be fully implemented by the current state-of-the-art
461 hygrothermal numerical models.

462

463 **4 Conclusions**

464 Three new mesoporous desiccant materials (MCM-41@165, SBA-15 6 nm and SBA-15 10
465 nm) were successfully synthesised with pore size modulation, in order to experimentally
466 recreate the ideal isotherms determined (for differing applications) by the hygrothermal model
467 optimization technique previously developed by the authors. A series of numerical
468 simulations were performed to assess the desiccants' capacity for regulating indoor RH and
469 the corresponding impact on energy efficiency when assisting a mixed mode AC system. The
470 simulated results clearly showed three stages of water vapour adsorption that strongly related
471 to the Δw gradient showing a positive linear correlation with the latent heat used for air
472 dehumidification. The results were also consistent with the predictions for progressive decay
473 and the point of failure, indicating the suitability of the materials for the p_v/p_0 scenarios for
474 which they had been designed. Increasing w did not result in lowering the energy used for
475 dehumidification purposes, especially for the Type III isotherm materials, and found no
476 correlation ($R^2 = 0.2706$) between total moisture storage, w and total latent heat for air
477 dehumidification. Experimental DVS and numerical simulation for water vapour
478 sorption/desorption kinetics were conducted for the three new materials, in which the latter
479 appeared to be slightly underestimated. This was consistent for most desiccants shown in
480 Figure 12 and Table 4, where the lack of a dynamic input for w (time-response for water
481 vapour adsorption), caused significant differences between both results. Additionally, Table 4
482 showed (see a, c, d, and g) that the major underestimations were largely attributed to a
483 combination of adsorption kinetics (time-response) and hysteresis. This, for the case of
484 MCM-41@165, was found to account for 52.4% (average) of the total w values at the third
485 RH buffering cycle. Conversely, it was found that the numerical model accurately predicted

486 EMC and found very good agreement with the experimental data taken from the water vapour
487 isotherm. Further research is therefore needed for coupling both adsorption kinetics (*i.e.*,
488 adsorption time–response) and realistic scanning curve estimates within the hysteresis loop.

489

490 **5 Acknowledgements**

491 The authors wish to gratefully acknowledge the support of CONICYT for funding this
492 research through the ‘Programa de Formación de Capital Humano Avanzado, BECAS
493 CHILE’ – Ministerio de Educación, Gobierno de Chile.

494

495 **6 References**

496

- 497 1. W. A. Belding, M. P. F. Delmas and W. D. Holeman, *Applied Thermal Engineering*,
498 1996, **16**, 447-459.
- 499 2. J. D. Chung and D.-Y. Lee, *International journal of refrigeration*, 2009, **32**, 720-726.
- 500 3. S. P. Casey, M. R. Hall, S. C. E. Tsang and M. A. Khan, *Building and Environment*,
501 2013, **60**, 24-36.
- 502 4. B. F. Yu, Z. B. Hu, M. Liu, H. L. Yang, Q. X. Kong and Y. H. Liu, *International*
503 *journal of refrigeration*, 2009, **32**, 3-20.
- 504 5. J. M. Calm, *International journal of refrigeration*, 2002, **25**, 293-305.
- 505 6. J. T. McMullan, *International journal of refrigeration*, 2002, **25**, 89-99.
- 506 7. S. B. Riffat, C. F. Afonso, A. C. Oliveira and D. A. Reay, *Applied Thermal*
507 *Engineering*, 1997, **17**, 33-42.
- 508 8. G. Lorentzen, *International journal of refrigeration*, 1995, **18**, 190-197.
- 509 9. *U.S. Pat.*, 5 580 369, 1996.
- 510 10. *U.S. Pat.*, 5 816 065, 1998.
- 511 11. A. A. Kinsara, M. M. Elsayed and O. M. Al-Rabghi, *Applied Thermal Engineering*,
512 1996, **16**, 791-806.
- 513 12. Y. J. Dai, R. Z. Wang, H. F. Zhang and J. D. Yu, *Applied Thermal Engineering*, 2001,
514 **21**, 1185-1202.
- 515 13. N. Srivastava and I. Eames, *Applied Thermal Engineering*, 1998, **18**, 707-714.

- 516 14. K. Daou, R. Wang and Z. Xia, *Renewable and Sustainable Energy Reviews*, 2006, **10**,
517 55-77.
- 518 15. D. La, Y. Dai, Y. Li, R. Wang and T. Ge, *Renewable and Sustainable Energy*
519 *Reviews*, 2010, **14**, 130-147.
- 520 16. L. Zhang and J. Niu, *Applied Thermal Engineering*, 2002, **22**, 1347-1367.
- 521 17. N. C. Srivastava and I. W. Eames, *Applied Thermal Engineering*, 1998, **18**, 707-714.
- 522 18. M. O'Kelly, M. E. Walter and J. R. Rowland, *Energy and Buildings*, 2015, **86**, 45-57.
- 523 19. P. Dhar and S. Singh, *Applied Thermal Engineering*, 2001, **21**, 119-134.
- 524 20. S. Jain, P. Dhar and S. Kaushik, *International journal of refrigeration*, 1995, **18**, 287-
525 296.
- 526 21. J. Camargo, E. Godoy Jr and C. Ebinuma, *Journal of the Brazilian Society of*
527 *Mechanical Sciences and Engineering*, 2005, **27**, 243-247.
- 528 22. P. Mazzei, F. Minichiello and D. Palma, *Applied Thermal Engineering*, 2005, **25**, 677-
529 707.
- 530 23. P. Mazzei, F. Minichiello and D. Palma, *Applied Thermal Engineering*, 2002, **22**, 545-
531 560.
- 532 24. M. R. Hall, ed., *Materials for energy efficiency and thermal comfort in buildings*,
533 CRC Press, Cambridge, 2010.
- 534 25. G. Panaras, E. Mathioulakis and V. Belessiotis, *Energy*, 2011, **36**, 2399-2406.
- 535 26. G. Grossman, *Solar Energy*, 2002, **72**, 53-62.
- 536 27. C. A. Balaras, G. Grossman, H.-M. Henning, C. A. Infante Ferreira, E. Podesser, L.
537 Wang and E. Wiemken, *Renewable and Sustainable Energy Reviews*, 2007, **11**, 299-
538 314.
- 539 28. A. E. Kabeel, *Renewable Energy*, 2007, **32**, 1842-1857.
- 540 29. M. Steeman, A. Janssens and M. De Paepe, *Applied Thermal Engineering*, 2009, **29**,
541 2870-2875.
- 542 30. M. Goldsworthy and S. White, *International journal of refrigeration*, 2011, **34**, 148-
543 158.
- 544 31. S. Henninger, F. Schmidt and H.-M. Henning, *Applied Thermal Engineering*, 2010,
545 **30**, 1692-1702.
- 546 32. F. Ziegler, *International journal of refrigeration*, 2002, **25**, 450-459.
- 547 33. R. Z. Wang and R. G. Oliveira, *Progress in Energy and Combustion Science*, 2006,
548 **32**, 424-458.
- 549 34. H. Demir, M. Mobedi and S. Ülkü, *Renewable and Sustainable Energy Reviews*, 2008,
550 **12**, 2381-2403.

- 551 35. J. Nie, L. Fang, G. Zhang, Y. Sheng, X. Kong, Y. Zhang and B. W. Olesen, *Building*
552 *and Environment*, 2015, **85**, 233-242.
- 553 36. E. Hürdoğan, O. Büyükalaca, M. Tolga Balta, A. Hepbasli and T. Yılmaz, *Energy*
554 *Conversion and Management*, 2013, **69**, 9-16.
- 555 37. X. Zheng, T. Ge and R. Wang, *Energy*, 2014, **74**, 280-294.
- 556 38. M. R. Hall, S. C. E. Tsang, S. P. Casey, M. A. Khan and H. Yang, *Acta Materialia*,
557 2012, **60**, 89-101.
- 558 39. S. T. Meek, J. A. Greathouse and M. D. Allendorf, *Advanced Materials*, 2011, **23**,
559 249-267.
- 560 40. H. Furukawa, N. Ko, Y. B. Go, N. Aratani, S. B. Choi, E. Choi, A. Ö. Yazaydin, R. Q.
561 Snurr, M. O’Keeffe and J. Kim, *Science*, 2010, **329**, 424-428.
- 562 41. R. Banerjee, A. Phan, B. Wang, C. Knobler, H. Furukawa, M. O’Keeffe and O. M.
563 Yaghi, *Science*, 2008, **319**, 939-943.
- 564 42. J. L. C. Rowsell and O. M. Yaghi, *Microporous and Mesoporous Materials*, 2004, **73**,
565 3-14.
- 566 43. W. Sangchoom and R. Mokaya, *Journal of Materials Chemistry*, 2012, **22**, 18872-
567 18878.
- 568 44. A. Corma, Q. Kan, M. T. Navarro, J. Pérez-Pariente and F. Rey, *Chemistry of*
569 *Materials*, 1997, **9**, 2123-2126.
- 570 45. A. Sayari and S. Hamoudi, *Chemistry of Materials*, 2001, **13**, 3151-3168.
- 571 46. J. Lei, J. Fan, C. Yu, L. Zhang, S. Jiang, B. Tu and D. Zhao, *Microporous and*
572 *Mesoporous Materials*, 2004, **73**, 121-128.
- 573 47. R. Collier, T. Cale and Z. Lavan, *Advanced desiccant materials assessment*,
574 Enerscope, Inc., Glendale, AZ (USA), 1986.
- 575 48. J. Canivet, A. Fateeva, Y. Guo, B. Coasne and D. Farrusseng, *Chemical Society*
576 *Reviews*, 2014.
- 577 49. P. Küsgens, M. Rose, I. Senkovska, H. Fröde, A. Henschel, S. Siegle and S. Kaskel,
578 *Microporous and Mesoporous Materials*, 2009, **120**, 325-330.
- 579 50. J. Ehrenmann, S. K. Henninger and C. Janiak, *European Journal of Inorganic*
580 *Chemistry*, 2011, **2011**, 471-474.
- 581 51. S. K. Henninger, H. A. Habib and C. Janiak, *Journal of the American Chemical*
582 *Society*, 2009, **131**, 2776-2777.
- 583 52. H. Furukawa, F. Gándara, Y.-B. Zhang, J. Jiang, W. L. Queen, M. R. Hudson and O.
584 M. Yaghi, *Journal of the American Chemical Society*, 2014, **136**, 4369-4381.
- 585 53. A. Khutia, H. U. Rammelberg, T. Schmidt, S. Henninger and C. Janiak, *Chemistry of*
586 *Materials*, 2013, **25**, 790-798.

- 587 54. G. Akiyama, R. Matsuda, H. Sato, A. Hori, M. Takata and S. Kitagawa, *Microporous*
588 *and Mesoporous Materials*, 2012, **157**, 89-93.
- 589 55. Y. K. Seo, J. W. Yoon, J. S. Lee, Y. K. Hwang, C. H. Jun, J. S. Chang, S. Wuttke, P.
590 Bazin, A. Vimont and M. Daturi, *Advanced Materials*, 2012, **24**, 806-810.
- 591 56. F. S. Thomann, M. R. Hall, W. Sangchoom and R. Mokaya, *Microporous and*
592 *Mesoporous Materials*, 2015, **211**, 113-123.
- 593 57. J. Rouquerol, F. Rouquerol and K. S. W. Sing, *Absorption by powders and porous*
594 *solids*, Academic press, Marseille, 1998.
- 595 58. H. M. Künzel, Ph.D. Thesis, IRB-Verlag, 1995.
- 596 59. D. Zhao, J. Feng, Q. Huo, N. Melosh, G. H. Fredrickson, B. F. Chmelka and G. D.
597 Stucky, *Science*, 1998, **279**, 548-552.
- 598 60. N. M. M. Ramos, J. M. P. Q. Delgado and V. P. de Freitas, *Construction and Building*
599 *Materials*, 2010, **24**, 2590-2597.
- 600 61. M. Woloszyn and C. Rode, *Building Simulation*, 2008, **1**, 5-24.
- 601 62. T. Kalamees and J. Vinha, *Building and Environment*, 2003, **38**, 689-697.
- 602 63. Z. Pavlík and R. Černý, *Energy and Buildings*, 2008, **40**, 673-678.
- 603 64. H. M. Künzel, A. Holm, D. Zirkelbach and A. N. Karagiozis, *Solar Energy*, 2005, **78**,
604 554-561.
- 605 65. B. EN, *German version DIN EN*, 2007, **15026**.
- 606 66. S. K. Henninger, F. Jeremias, H. Kummer and C. Janiak, *European Journal of*
607 *Inorganic Chemistry*, 2012, **2012**, 2625-2634.
- 608 67. H. Naono, M. Hakuman, T. Tanaka, N. Tamura and K. Nakai, *Journal of Colloid and*
609 *Interface Science*, 2000, **225**, 411-420.
- 610 68. Z. Knez and Z. Novak, *Journal of Chemical & Engineering Data*, 2001, **46**, 858-860.
- 611 69. W. Wang, L. Wu, Z. Li, Y. Fang, J. Ding and J. Xiao, *Drying Technology*, 2013, **31**,
612 1334-1345.
613
614
615
616
617
618
619

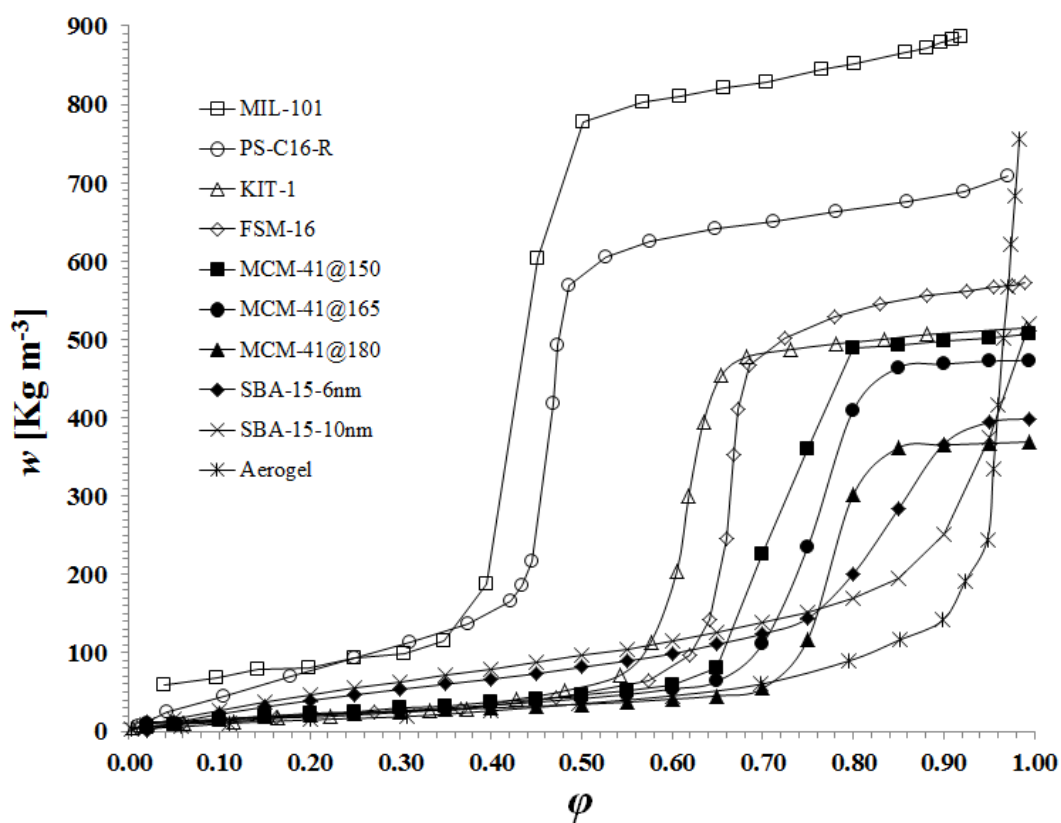


Figure 1 – Water vapour sorption isotherms for all desiccant candidates. References are provided for the following desiccants candidates: MIL-101⁶⁶, PS-C16-R⁶⁷, KIT-1 and FSM-16⁶⁹, MCM-41@150 and 180³⁸, Aerogel⁶⁸. The three water vapour isotherms from the new materials made (MCM-41@165, SBA-15 6 nm and 10 nm) are also provided.

620

621

622

623

624

625

626

627

628

629

630

631

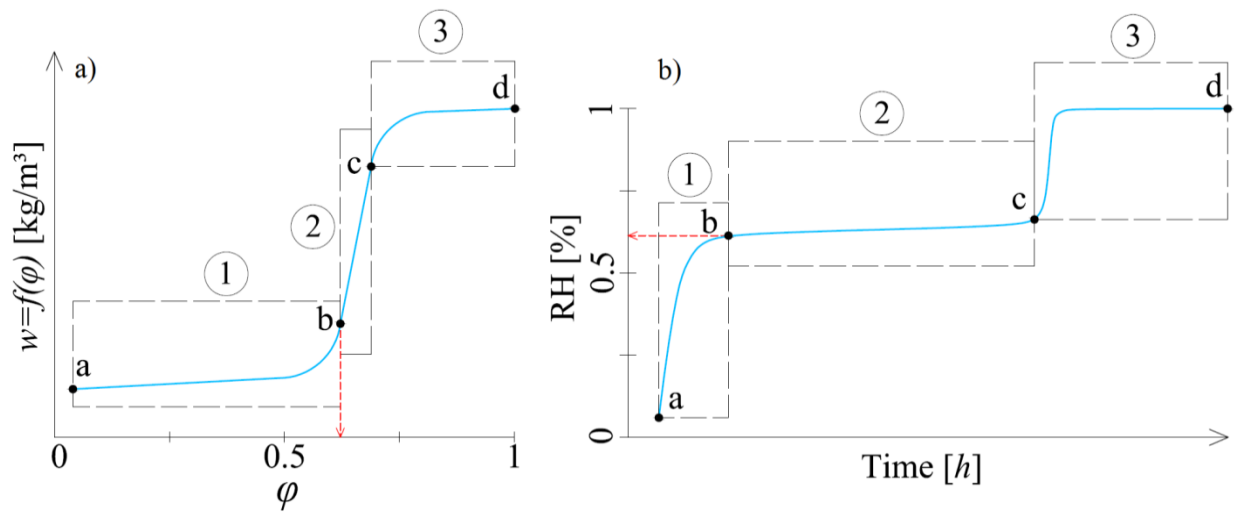


Figure 2 – (a) Schematic representation of a water vapour sorption isotherm portions at different EMC stages a-b, b-c and c-d. (b) Corresponding water vapour sorption kinetics at different EMC stages a-b, b-c and c-d that shows EMC in the segments 1, 2 and 3.

632

633

634

635

636

637

638

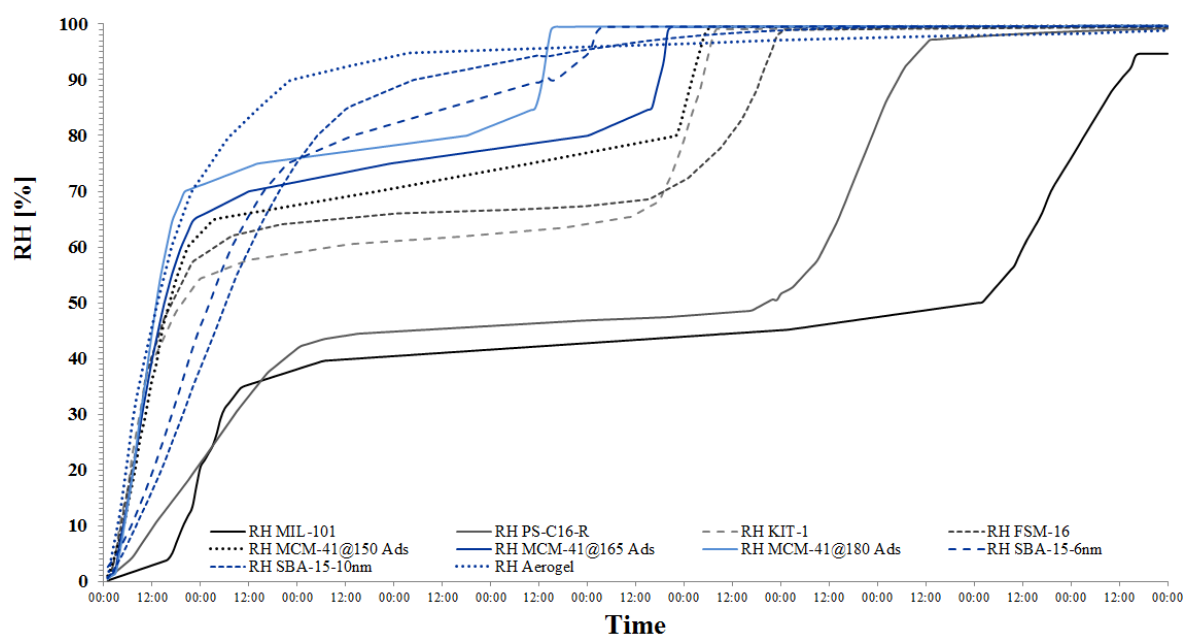


Figure 3 – Water vapour sorption kinetic stages for all desiccant candidates when achieving EMC_{100} . Initial $w = 0$ for all desiccant materials and the moisture load applied is the moisture content of the infiltrated air at $ACH = 0.35^{-1}$, where $\varphi_e = 0.95$.

639

640

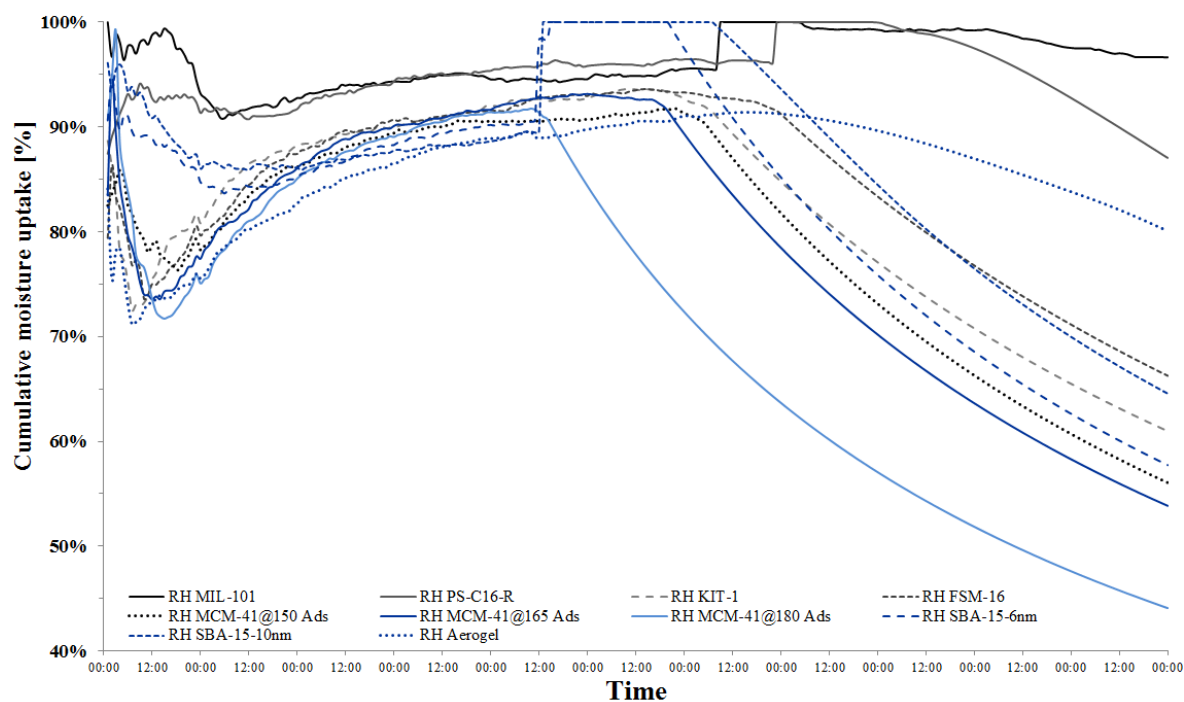


Figure 4 – Cumulative water vapour uptake for all desiccant candidates. Initial $w = 0$ for all desiccant materials and the moisture load applied is the moisture content of the infiltrated air at $\text{ACH} = 0.35^{-1}$, where $\varphi_e = 0.95$.

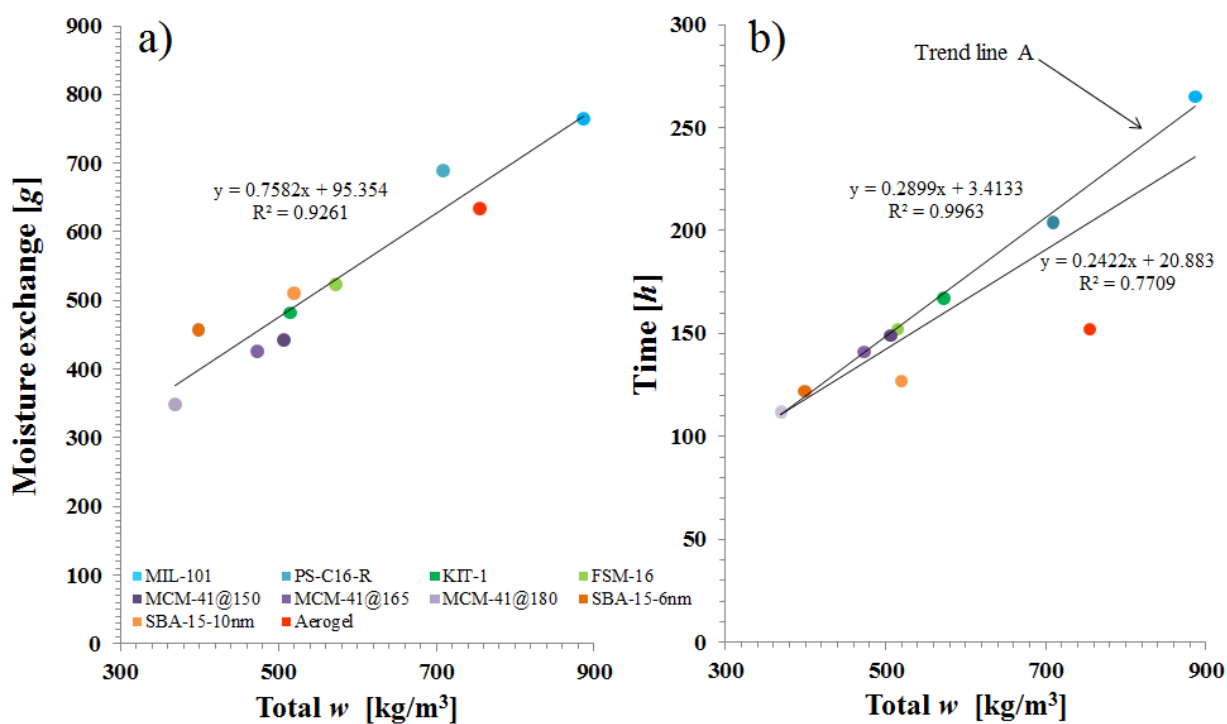


Figure 5 – (a) Linear correlation between the moisture storage capacity, w and the water vapour being exchanged. (b) Relationship between total moisture storage capacity and time taken to achieve EMC₁₀₀.

641

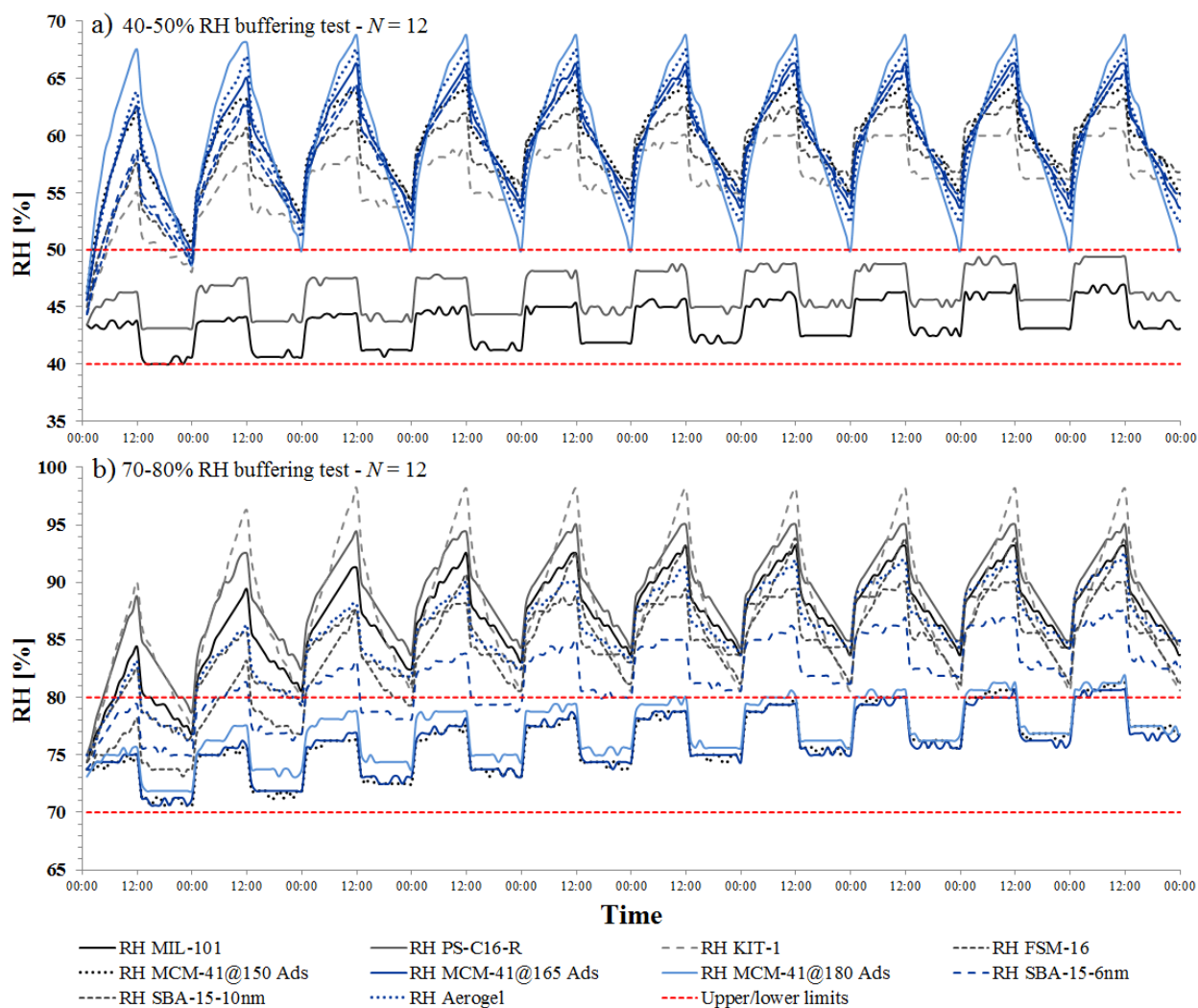


Figure 6 – RH buffering results for all desiccant candidates, where the number of cycles, $N = 12$. (a) Shows the simulations results for RH buffering between 40–50%, and (b) 70–80% operating ranges. The red-dotted lines correspond to the maximum and minimum RH limits.

642

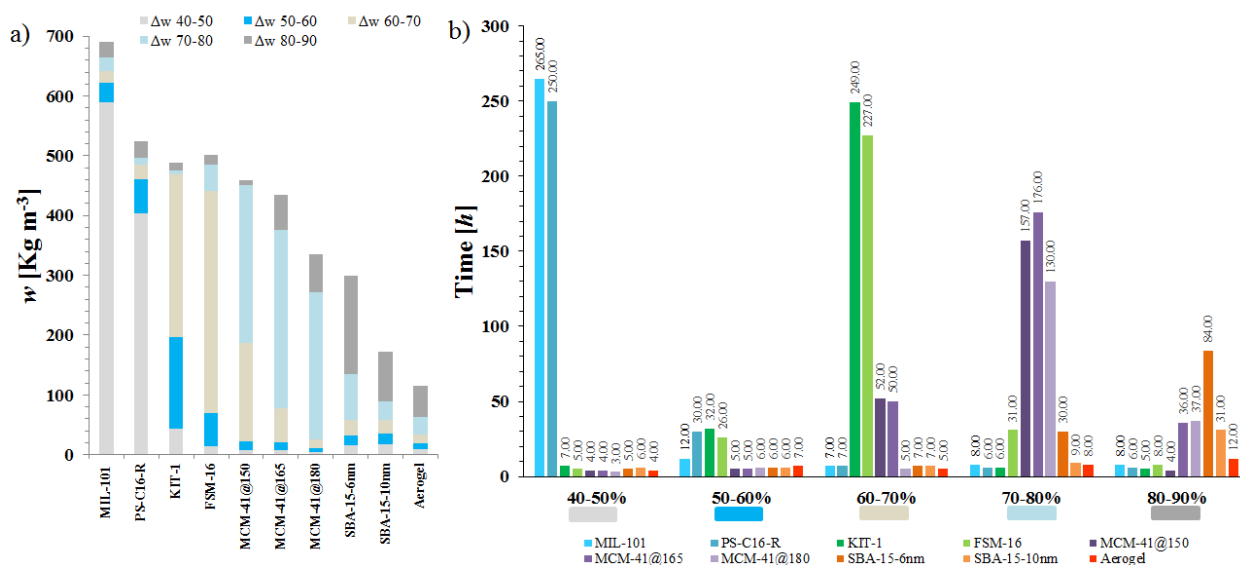


Figure 7 – (a) Water vapour uptake capacity at different Δw for all desiccant candidates ($\Delta w = 40-50$; $50-60$; $60-70$; $70-80$; and $80-90$). (b) Time taken for all desiccant materials when the fluctuation of $\varphi(t)$ exceeds the φ_{max} limit, where $\Delta w = 40-50$; $50-60$; $60-70$; $70-80$; and $80-90$. This also correspond to the threshold when the materials reaches failure at the number of cycles, $N = 60$.

643

644

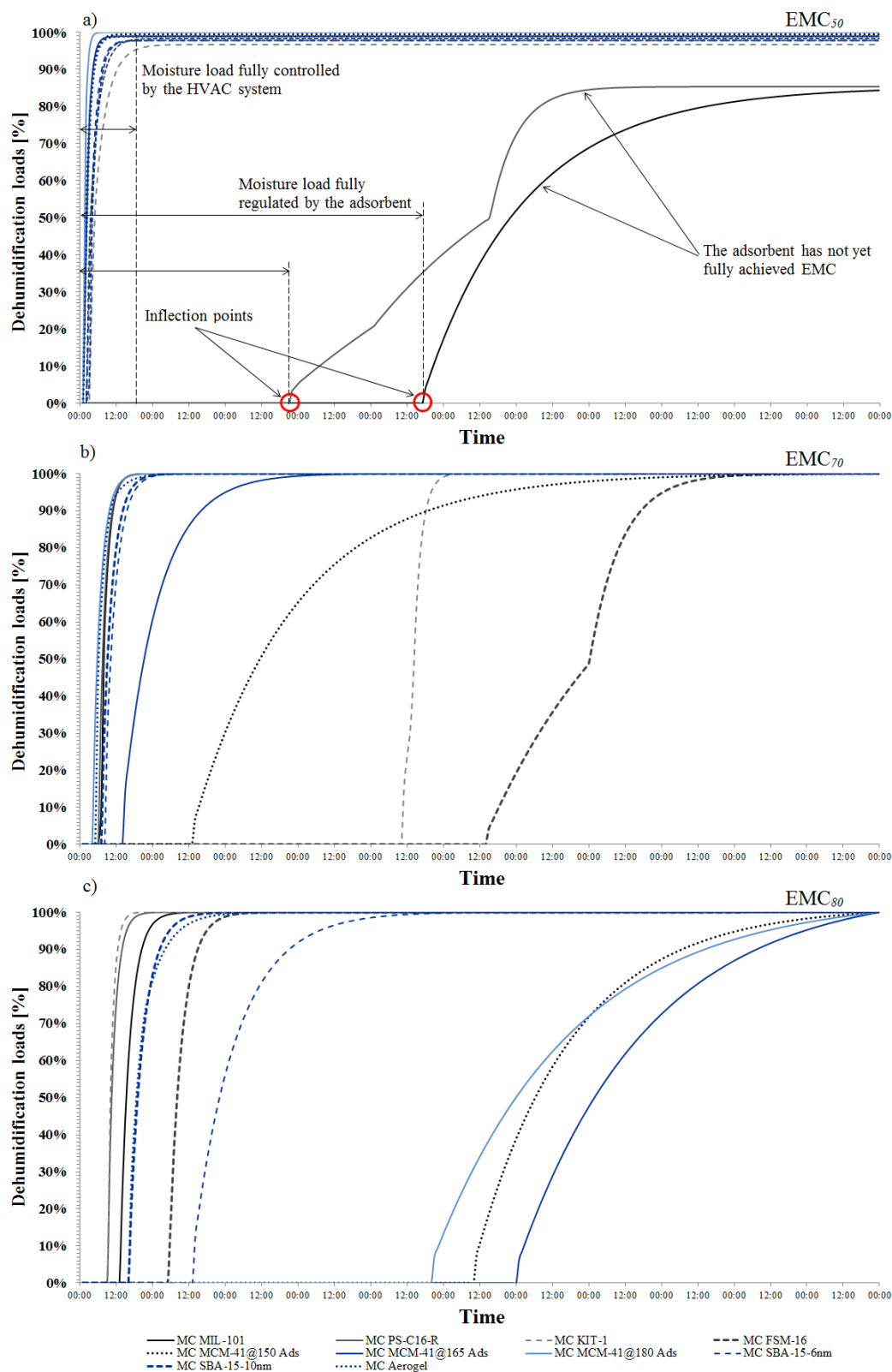


Figure 8 – Dehumidification ratio performed by the HVAC system and the desiccant candidates according to the operating ranges (a) 40–50; (b) 60–70; and (c) 70–80 % RH. Here, 0% indicates that the desiccant candidate is fully regulating indoor RH. Above 0% indicates that the HVAC system start to working in truly mixed mode. The time taken for reaching EMC at the corresponding operating ranges are solely dependent upon the Δw gradient.

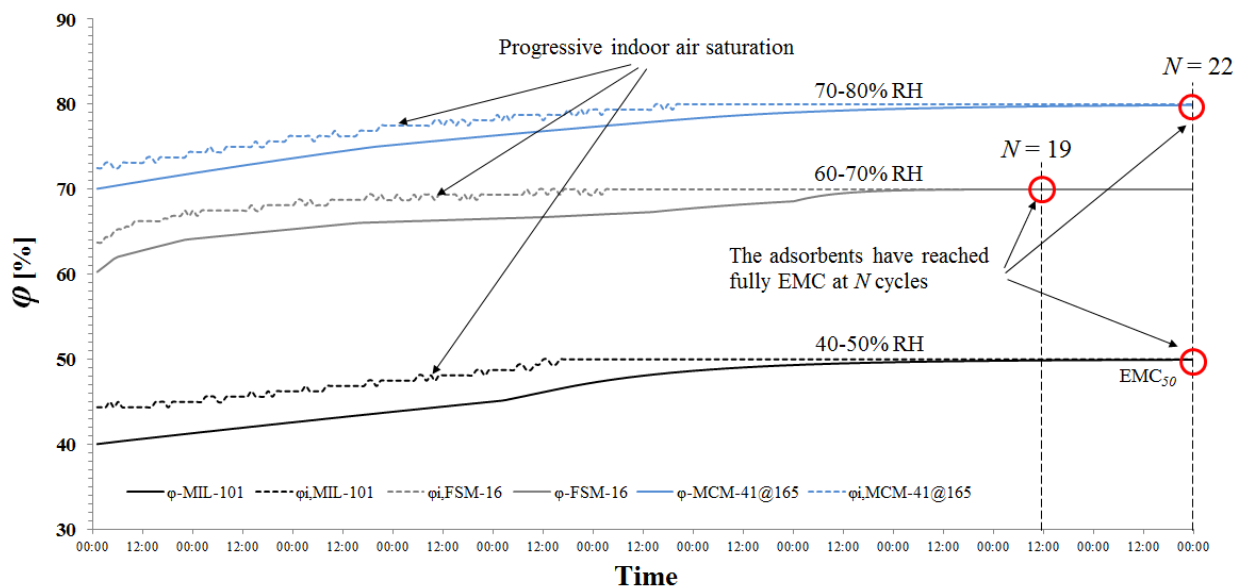


Figure 9 – Comparison between the resultant indoor $RH(t)$ and the material's $RH(t)$ at different operating ranges for desiccant materials MIL-101, FSM-16 and MCM-41@165. The offset dotted-lines represent the progressive indoor air saturation towards equilibrium with the desiccant at the respective ACH^{-1} . The total number of cycles, $N = 22$ and the red circles represents when the desiccants have been reached EMC at the corresponding operating RH ranges.

645

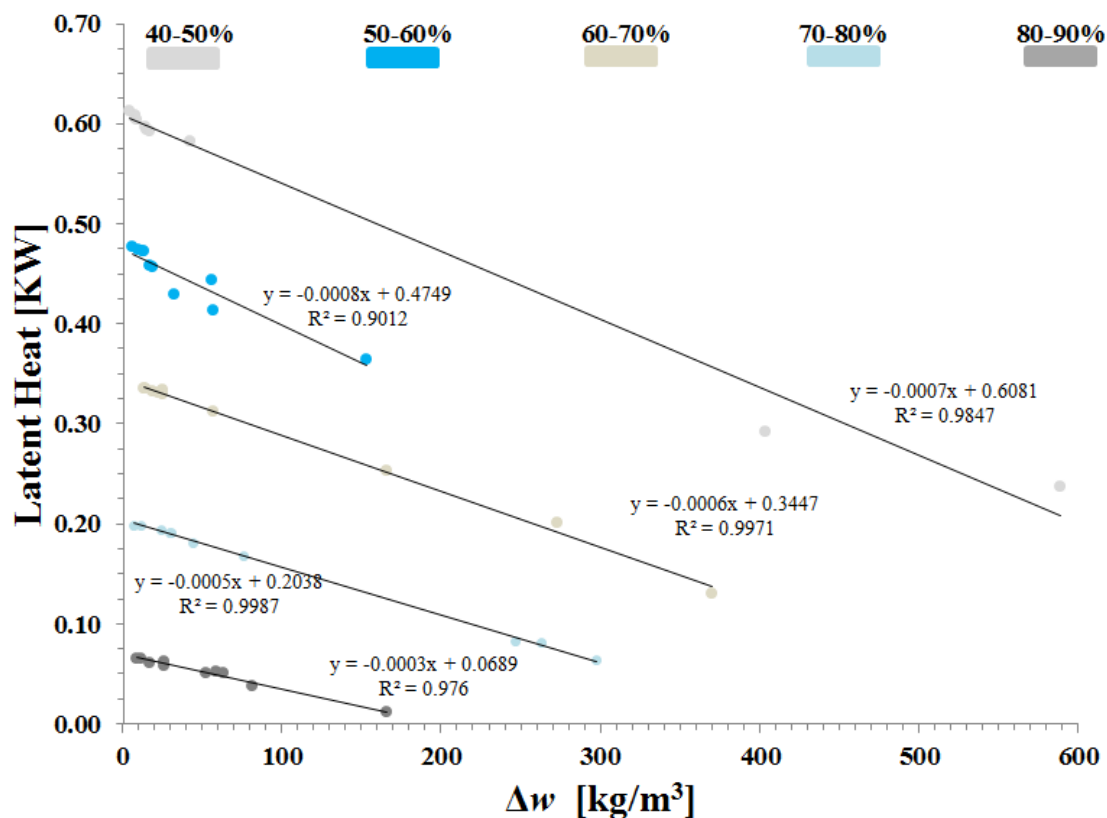


Figure 10 – Correlation between moisture sorption capacity and the latent heat used for air dehumidification from the HVAC system at the corresponding operating ranges (40-50%; 50-60%; 60-70%; 70-80%; 80-90%). Each trend line correspond to the aggrupation of all desiccant candidates when performing the air dehumidification through the HVAC system.

646

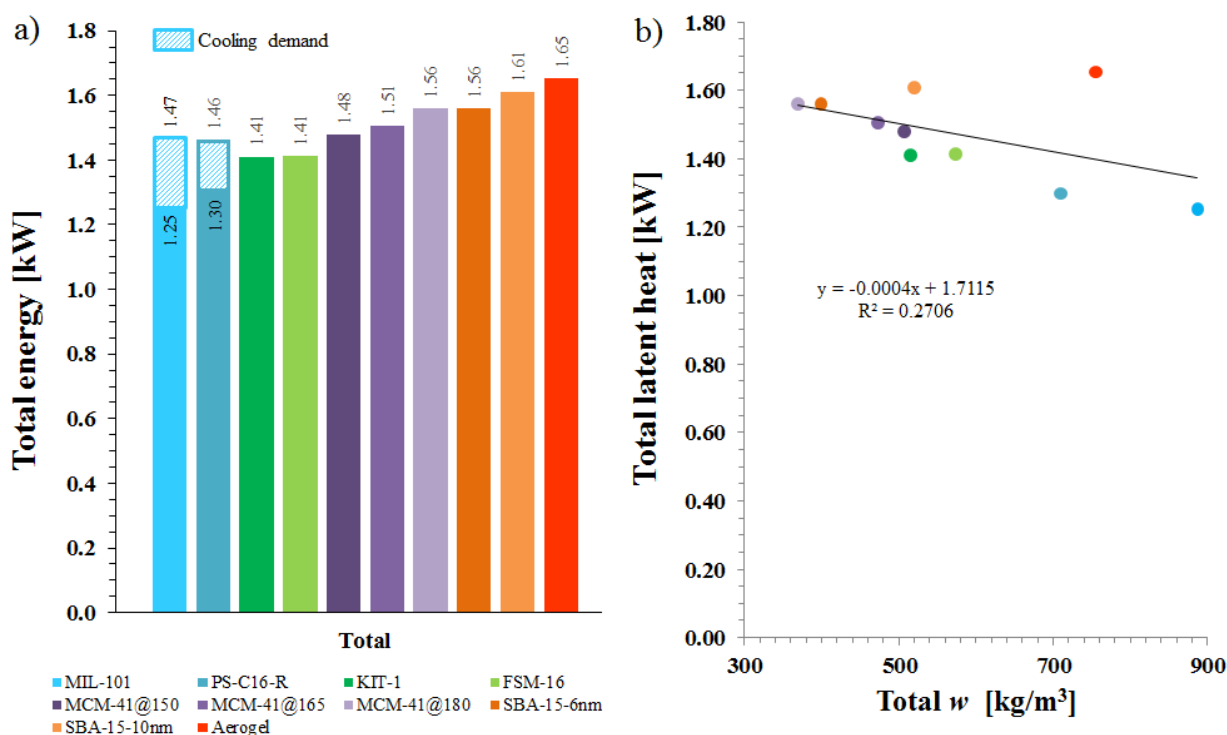


Figure 11 – (a) Total energy used for air dehumidification for all desiccant candidates. In the case of materials MIL-101 and PS-C16-R, a cooling demand is represented by the hatched box above the values. (b) Non-linear correlation between total moisture storage, w and total latent heat for air dehumidification. Type III isotherms can clearly be recognized as the precursors of this non-linear trend as their total moisture content, w do not correlate with the total energy used for air dehumidification and cooling loads, resulting in $R^2 = 0.2706$.

647

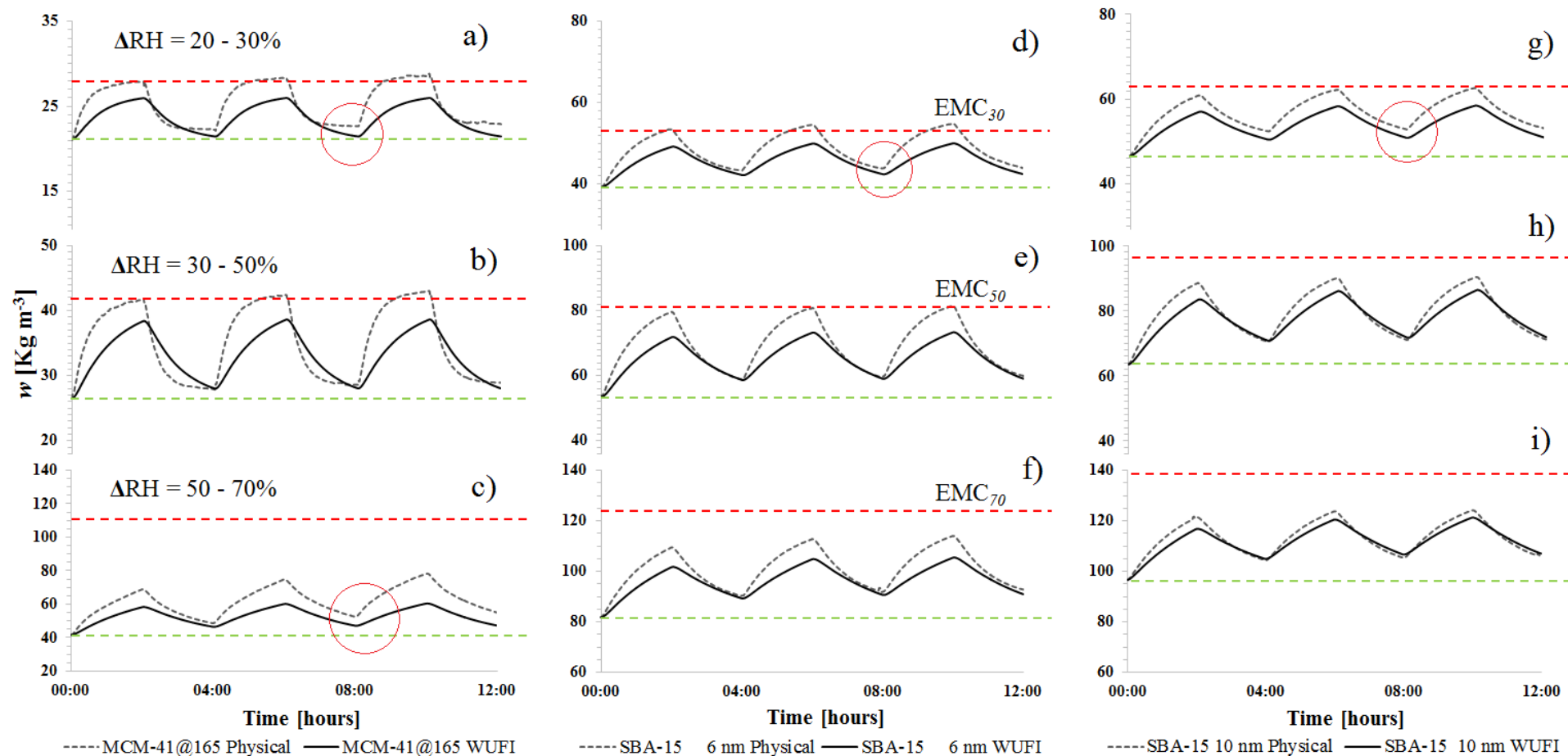


Figure 12 – Water vapour sorption/desorption kinetics comparison between experimental DVS and numerical simulations. The results are deemed to be read horizontally, where A) indicates the operating range $\Delta\text{RH} = 20\text{-}30\%$; B) $\Delta\text{RH} = 30\text{-}50\%$; and C) $\Delta\text{RH} = 50\text{-}70\%$. The red-dotted lines indicate achieving the corresponding EMC, whereas the green-dotted lines indicate the base line for the initial w .

648
649
650

Sample	$S_{\text{BET}}/\text{m}^2\text{g}^{-1}$	$V_{\text{m}}/\text{cm}^3\text{g}^{-1}$	$V_{\text{p}}/\text{cm}^3\text{g}^{-1}$	D_{p}/nm
SBA-15 6 nm	876	0.17	0.91	5.7
SBA-15 10 nm	757	0.12	1.26	10.2

651 **Table 1** – Textural properties summary for SBA-15 desiccant candidates.

652

Material	n	ϕ_{pore}	ρ_{b}	C_{p}	λ	A	μ
	(m^3/m^3)	(nm)	(kg/m^3)	(J/kg K)	(W/m.K)	($\text{kg}/\text{m}^2 \text{s}^{0.5}$)	(-)
MS-8.3*	0.76	8.3	618	1691	0.05	0.550	10.52

653 **Table 2** – Hygrothermal functional properties for mesoporous silica. *Values taken from
654 reference ³⁸.

655

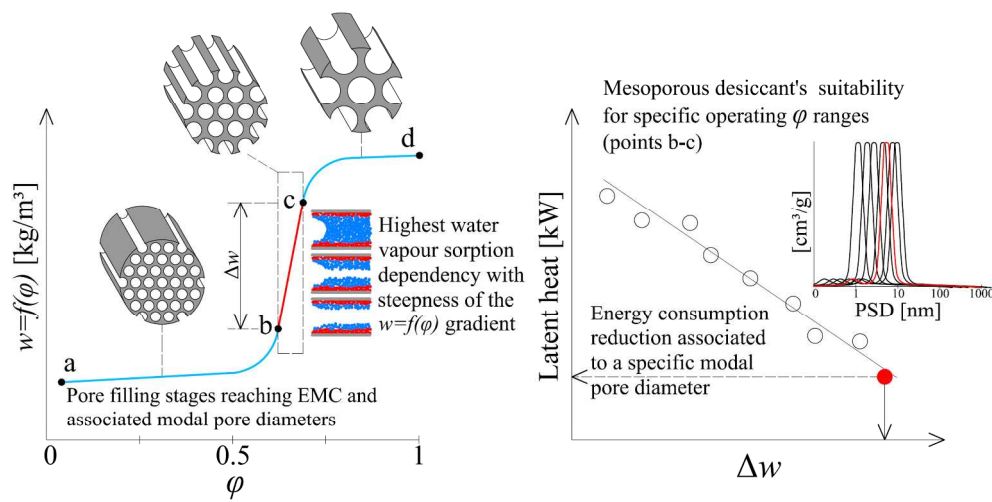
Desiccant materials	Moisture storage at Δw			Time in achieving EMC		
	Δw_{20-30}	Δw_{30-50}	Δw_{50-70}	Δw_{20-30}	Δw_{30-50}	Δw_{50-70}
	(kg/m ³)			(~ h)		
MCM-41@165	5.4	15.1	69.8	3	5.5	22
SBA-15 6nm	14.2	28.3	42.5	5	9.5	11
SBA-15 10nm	16.8	33.1	41.8	6	11	11

Table 3 – Moisture storage capacity at different Δw for all new desiccant materials. The time in achieving EMC is also presented with an approximate time (h) for each desiccant at the corresponding ranges: Δw_{20-30} ; Δw_{30-50} ; and Δw_{50-70} . These time values represent numerical predictions based on w inputs that are assumed to be at full EMC.

Cycles	Mesoporous desiccant materials								
	MCM-41@165			SBA-15 6 nm			SBA-15 10 nm		
	Δw_{20-30}	Δw_{30-50}	Δw_{50-70}	Δw_{20-30}	Δw_{30-50}	Δw_{50-70}	Δw_{20-30}	Δw_{30-50}	Δw_{50-70}
	a	b	c	d	e	f	g	h	i
Ads. cycle 1	44.4%	43.3%	48.4%	44.4%	43.6%	39.8%	40.0%	35.2%	27.8%
Des. cycle 1	11.3%	-56.6%	28.2%	16.9%	6.5%	13.0%	24.9%	1.7%	3.0%
Ads. cycle 2	48.8%	40.5%	45.9%	38.2%	32.2%	28.6%	33.1%	18.5%	11.5%
Des. cycle 2	29.4%	-27.9%	41.8%	21.3%	7.3%	12.0%	23.2%	-3.7%	-4.2%
Ads. cycle 3	51.8%	43.4%	52.4%	38.1%	33.4%	29.0%	32.7%	16.6%	7.6%
Des. cycle 3	36.3%	-15.0%	49.2%	23.9%	11.0%	14.8%	24.1%	-3.7%	-4.6%

Table 4 – Average difference (%) between experimental and numerical w data for all new mesoporous desiccant materials, when modelling for each independent RH buffering scenario 20–30 % RH; 30–50 % RH; and 50–70 % RH. The w differences are provided for the following ranges: Δw_{20-30} ; Δw_{30-50} ; and Δw_{50-70} , denoted with the vowels (a–i) according to Figure 12, and for the three completed adsorption/desorption cycles.

656
657
658
659
660
661
662
663
664
665



603x318mm (96 x 96 DPI)